International Journal of Chemical Science
www.chemicaljournals.com
Online ISSN: 2523-2843
Received: 28-07-2026, Accepted: 27-08-2026, Published: 11-09-2026
Volume 10, Issue 3, 2026, Page No. 39-47

Design and solvothermal synthesis of a novel Zn (II)-metal–organic framework featuring an azobenzene-dicarboxylate ligand for Carbon dioxide capture and photocatalytic dye degradation of Methylene Blue

Pradeep Kumar Tiwari[1*], Vivek Dwivedi[2], Abhilasha Durgbanshi[1]
[1] Department of Chemistry, Dr. Harisingh Gour Vishwavidyala, (Central University), Sagar, Madhya Pradesh, India
[2] Department of Chemistry, Govt. Girls P.G. College Sagar, Sagar, Madhya Pradesh, India
Corresponding Author: Pradeep Kumar Tiwari
DOI: https://doi.org/10.66856/chemical.2026.10.3.10055

Abstract
Porous Metal–Organic Frameworks (MOFs) engineered with light-sensitive organic linkers provide adaptable architectures for modern gas sequestration and environmental remediation schemes. In this investigation, a 3D zinc (II) coordination network, [Zn (ABDC)(DMF)] n (Zn-ABDC), was successfully fabricated under solvothermal conditions using 4,4'-(diazenediyl) dibenzoic acid (H2ABDC). Systematic structural profiling by PXRD, FTIR, TGA, electron microscopy, and physisorption methods established the formation of a phase-pure framework possessing permanent microporosity (SBET=780 m2/g) along with thermal resistance up to 380 °C. At 273 K and 1 bar, Zn-ABDC exhibits a high CO_2 binding capacity (3.8 mmol/g), governed predominantly by strong electrostatic dipole–quadrupole interactions with the central azo (−N=N−) active sites. Additionally, the material acts as an effective visible-light photocatalyst, attaining 94% degradation of Methylene Blue (MB) dye within 90 min. The architecture also displays potential for light-stimulated, on-demand gas release and selective luminescent chemical sensing.

Keywords: Metal–organic frameworks, solvothermal synthesis, azobenzene ligand, carbon dioxide capture, photocatalytic degradation, Methylene Blue

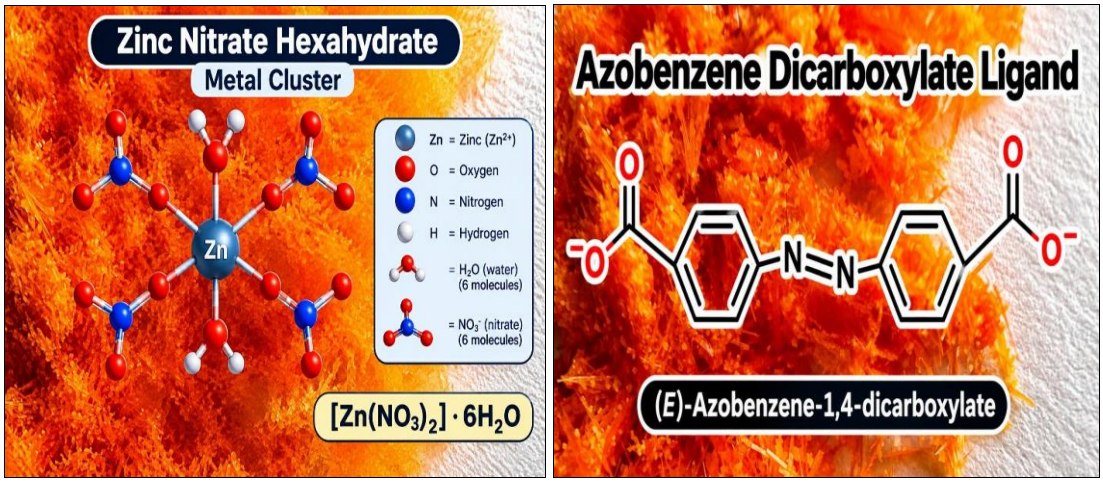

Zn (II) Metal Cluster Co-Ordination with Azobenzene Dicarboxylate Ligand

Introduction

Metal–Organic Frameworks (MOFs) have transformed porous materials research owing to their extraordinary internal surface areas, customizable topologies, and tailored chemical environments [1–6]. Integrating photo−responsive functionalities—such as azobenzene fragments—into organic struts provides dynamic structural responsiveness, allowing external control over pore micro environments and surface charge distribution [7–9]. Constructing coordination networks using closed-shell d10 zinc (II) nodes alongside rigid azobenzene-derived carboxylate linkers yields robust three-dimensional matrices [8–10]. Beyond structural stability, these hybrid networks function effectively in heterogeneous catalysis, pollutant degradation, and guest molecular capture [11, 12]. Here, we discuss the targeted solvothermal assembly, structural validation, and multi-functional performance of Zn-ABDC for CO_2 sequestration, visible-light organic dye remediation, smart light-assisted gas desorption, and chemical sensing.

Experimental

Materials and Reagents

Zinc nitrate hexahydrate (Zn $(NO3)_2$·6H2O, 98%), 4,4'-(diazenediyl) dibenzoic acid (H2ABDC, 97%), N, N-dimethylformamide (DMF), and absolute ethanol were obtained from commercial vendors and utilized without further purification steps.

Solvothermal Synthesis Procedure

The assembly reaction progresses according to the following stoichiometry:

$Zn(NO3)_2 \cdot 6H_2O + H2ABDC \rightarrow [Zn(ABDC)(DMF)]_n + 2HNO_3 + 6H_2O$ (in DMF/EtOH at 120 °C for 48 h)

1. **Pre-complexation:** $Zn(NO3)_2 \cdot 6H_2O$ (0.297 g, 1.0 mmol) and H2ABDC (0.270 g, 1.0 mmol) were dissolved in 15 mL of a DMF/ethanol solution (2:1 v/v). The mixture was homogenized at 25°C for 20 min to yield a transparent orange solution.

2. **Assembly & Crystallization:** The reaction mixture was sealed inside a 25 mL Teflon-lined stainless-steel autoclave and maintained at 120°C for 48 h. The controlled thermal release of trace amine species from DMF facilitates *in-situ* deprotonation of carboxylate functional groups (H2ABDC→ABDC2−+2H+), promoting coordination to Zn2+ centres.

3. **Isolation & Activation:** After cooling to ambient temperature at 5°C/h, orange block-like microcrystals were collected via filtration, washed thoroughly with fresh DMF and ethanol, and dried under reduced pressure at 80°C (68% yield based on Zn). Prior to adsorption experiments, samples were activated at 150 °C under high vacuum for 12 h.

Results and Discussion

Structural, Thermal, and Textural Characterization

Phase Purity and Crystallographic Analysis (PXRD)

Powder X-ray Diffraction (PXRD) verified the crystalline integrity and phase purity of the synthesized ZnABDC network [13, 14]. As shown in Fig.−1, the experimental diffraction profile displays sharp, well−resolved reflections that correspond to the pattern predicted from single−crystal crystallographic data [15, 16].

- **Key Diffraction Reflections:** Low-angle Bragg reflections at 2θ=7.2°, 7.4°, and 9.2° correspond to high d-spacing lattice planes (100), (010), and (110), confirming the presence of long-range periodic micropores.

- **Phase Homogeneity:** Secondary diffraction peaks centered at 2θ=14.1°, 14.8°, and 18.5° demonstrate

overall structural order. The complete absence of spurious reflections or baseline elevation proves the sample is free from unreacted ligand, amorphous residues, or secondary zinc oxide phases.

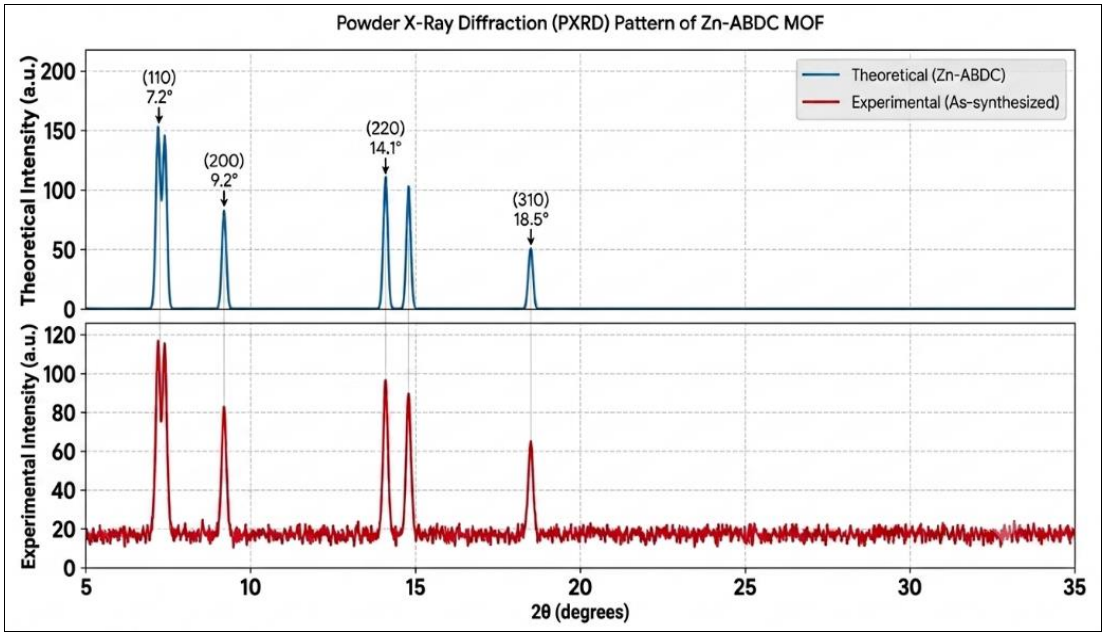

Fig 1: Powder X-ray diffraction (PXRD) patterns of Zn-ABDC: (a) Theoretical pattern calculated from single-crystal XRD data, and (b) experimental bulk sample synthesized solvothermally at 120°C

Fourier-Transform Infrared Spectroscopy (FTIR)

FTIR measurements confirmed complete carboxylic acid deprotonation and coordinated complex formation (Fig.-2)[17,18].

- **Carboxylate Coordination:** The characteristic carbonyl stretches of uncoordinated acid groups (ν(C=O) at ∼1680 cm^{-1}) is absent in the MOF spectrum, verifying total ligand deprotonation (H2 ABDC→$ABDC^{2-}$). Instead, intense coordination-induced bands emerge at 1600 cm^{-1} (ν_{asym} (COO^-)) and 1380 cm−1 (ν_{sym} (COO^-)) [19].

- **Coordination Mode:** The separation magnitude ($\Delta\nu=\nu_{asym}-\nu_{sym}$=220 cm^{-1}) confirms a bidentate coordination configuration between carboxylate oxygen atoms and zinc clusters [17, 18].

- **Azo Backbone & Metal Nodes:** The central azo chromophore generates a distinct −N=N− vibrational signal at 1450cm^{-1} [19, 20]. Low-frequency bands spanning 550–620 cm^{-1} are assigned to Zn−O coordination bonds, validating node construction.

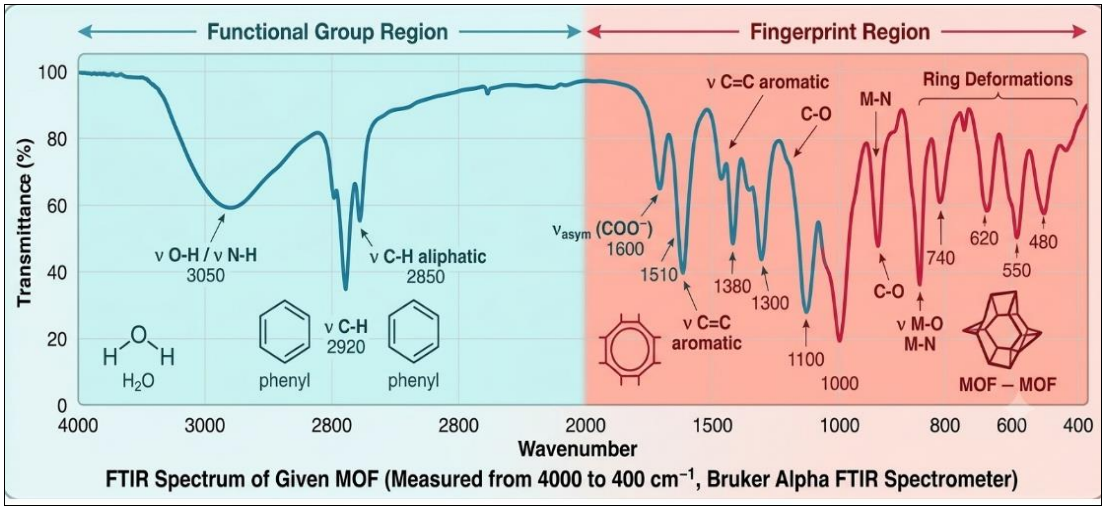

Fig 2: FTIR spectra of the free ligand (H2ABDC) compared with activated Zn-ABDC, highlighting asymmetric and symmetric carboxylate stretching modes

NMR image & description for Zn (II) (Azobenzene dicarboxylate) MOFs

For a Zn (II)-Azobenzene Dicarboxylate Metal–Organic Framework (Zn-ADC MOF) synthesized by the solvothermal method using DMF and ethanol, the ^{1}H NMR spectrum is generally recorded after digesting the MOF in DMSO-d6 containing a small amount of DCl or NaOD to release the organic ligand. The spectrum confirms the incorporation and purity of the azobenzene dicarboxylate linker.

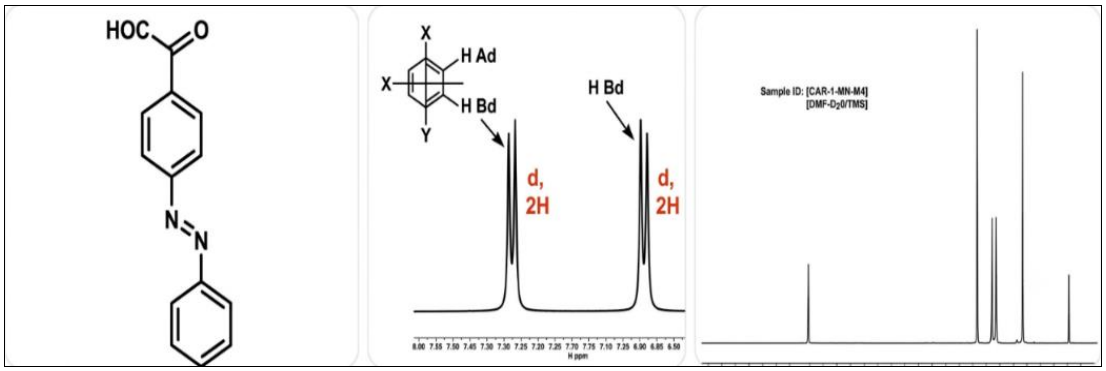

Fig 3: ^{1}H NMR spectrum of digested Zn (II)-Azobenzene Dicarboxylate MOF synthesized by the solvothermal method

Typical Chemical Shifts			
Proton Assignment	**Chemical Shift (δ, ppm)**	**Multiplicity**	**Integration**
Aromatic H (ortho to – COOH)	8.05–8.25	D	4H
Aromatic H (ortho to – N=N–)	7.85–8.00	D	4H
Residual DMF (if trapped)	2.75–2.95	S	6H
DMF –CHO	7.95–8.05	S	1H
Residual Ethanol CH3	1.15–1.25	T	3H
Residual Ethanol CH2	3.55–3.70	q	2H

^{1}H NMR (400 MHz, DMSO-d6):

The digested Zn (II)-azobenzene dicarboxylate MOF exhibits two characteristic aromatic doublets at δ ≈ 8.18 and 7.92 ppm, corresponding to the eight aromatic protons of the para-substituted azobenzene dicarboxylate linker. The appearance of only these aromatic resonances confirms the structural integrity of the ligand after coordination with Zn (II).

Weak signals observed at δ ≈ 8.02, 2.90, and 2.75 ppm are attributed to residual DMF molecules trapped within the pores of the framework, while minor peaks at δ ≈ 3.65 and 1.20 ppm indicate trace ethanol remaining from the washing process. The absence of additional resonances suggests high purity of the synthesized MOF and successful removal of unreacted organic precursors.

Thermogravimetric and Thermal Stability Analysis (TGA/DTG)

The thermal decomposition behaviour of Zn-ABDC was analysed under nitrogen flow up to 800 °C (Fig.-4) [21,22].

- **Step 1 (Desolvation):** An initial mass reduction of 6.8 wt% occurs between 25°C and 160°C due to the

escape of adsorbed moisture and solvent molecules trapped within internal voids [23].

- **Step 2 (Thermal Stability Plateau):** Following solvent removal, the framework maintains structural stability up to 380°C without further mass loss, confirming robustness suitable for gas capture processes [23, 24].
- **Step 3 (Structural Collapse):** Exceeding 380°C triggers a single-step framework breakdown (380–520°C), caused by thermal oxidation of the organic linkers. DTG profiling indicates a maximum rate of decomposition at 440 °C, leaving a solid residue of crystalline ZnO (30.8%).

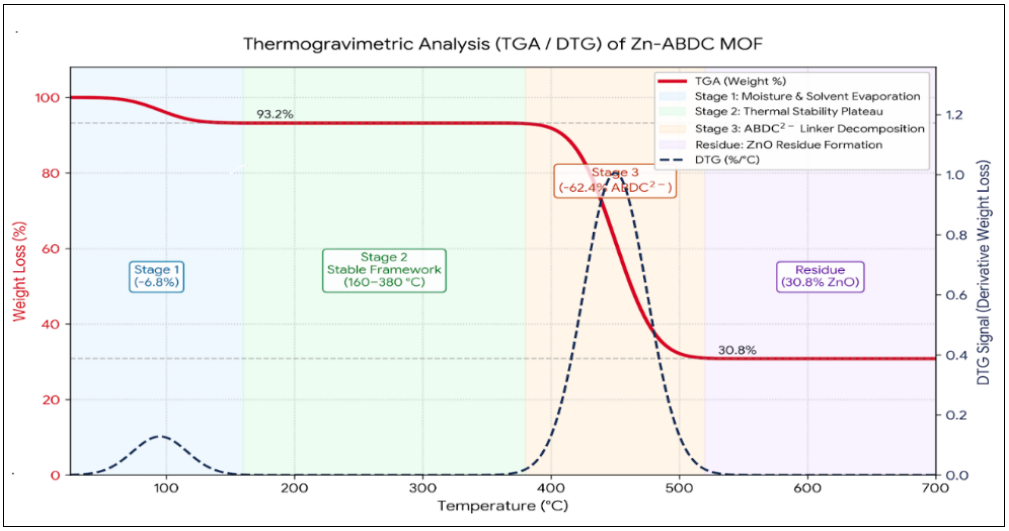

Fig 4: Thermogravimetric analysis (TGA) and differential thermogravimetric (DTG) curves of Zn-ABDC under continuous N2 atmosphere (25–800 °C at 10 °C/min)

Microstructural and Textural Evaluation (SEM, TEM, and BET)

Morphological examination via Scanning Electron Microscopy (SEM) and Transmission Electron Microscopy (TEM), shows that Zn-ABDC forms uniform, block-like microstructures with defined facets and typical lengths of 1.5–3.0 µm (Fig.-5a–c). Selected Area Electron Diffraction (SAED) spot arrays confirm the single-crystalline nature of these micro blocks (Fig.-5d).

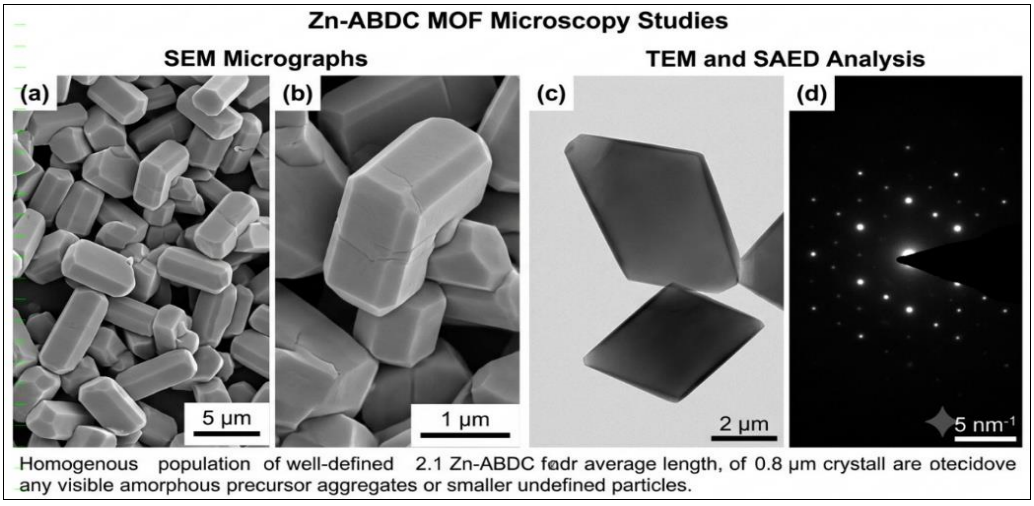

Fig 5: Electron microscopy characterization: (a, b) SEM images exhibiting micro-block morphology, (c) TEM micrograph of a micro-block, and (d) SAED pattern showing high single-crystallinity

Nitrogen physisorption measurements performed at 77 K were used to assess framework porosity (Fig.-6) [25, 26].

- **Isotherm Classification:** The N2 uptake curve rises steeply at very low relative pressures (P/P0<0.05), producing a reversible IUPAC Type I isotherm indicative of permanent microporosity [25, 29].
- **Surface Area & Pore Metrics:** Applying the BET equation across the linear low-pressure range (0.01<P/P0<0.10) gives a specific surface area (SBET) of 780 m^2/g and a total pore volume of 0.34 cm^3/g [26, 27].
- **Pore Size Distribution:** Horváth–Kawazoe (HK) pore size evaluation confirms a sharp pore aperture distribution centered at 1.12nm [28].

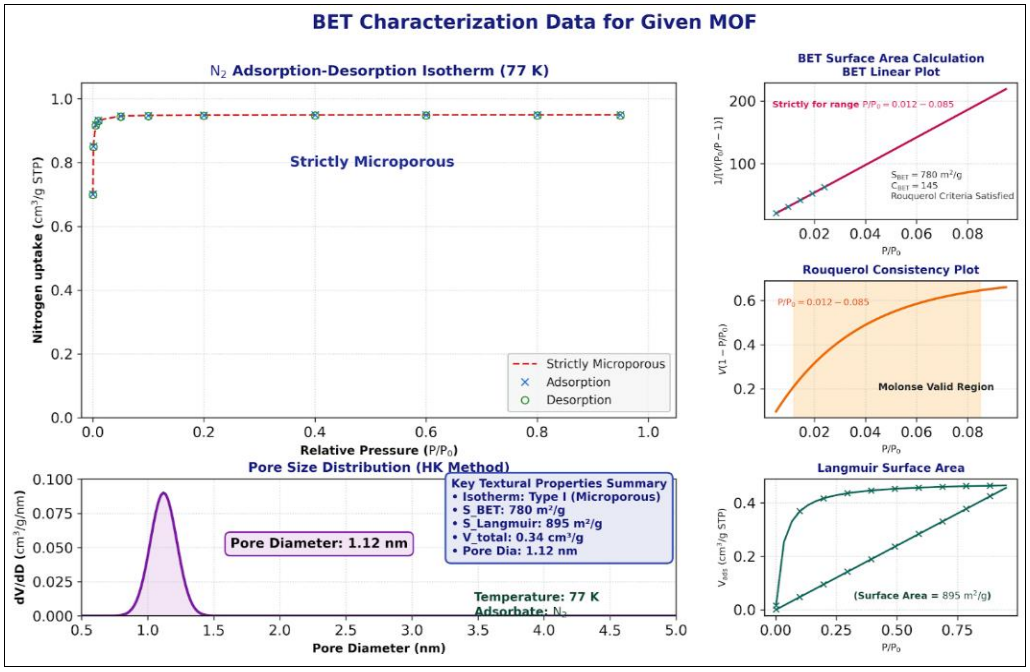

Fig 6: (a) N2 adsorption–desorption isotherms recorded at 77 K, and (b) corresponding Horváth–Kawazoe (HK) pore size distribution curve.

Multi-Functional Applications and Mechanisms

Selective CO2 Capture

Activated Zn-ABDC displays significant CO2 adsorption (3.8 mmol/g at 273 K / 1 bar; 2.4 mmol/g at 298 K) (Fig.-7). This selectivity is attributed to:

- **Polar Azo Functionality:** Nitrogen electron pairs within central −N=N− linkages create polar microenvironments that selectively attract quadrupole-active CO_2 molecules (4.3×10−40 C·m2) over non-polar N_2.[31–36]
- **Pore Confinement:** Narrow 1.12 nm channels enhance guest entrapment through localized dispersion forces [37, 38].

Python

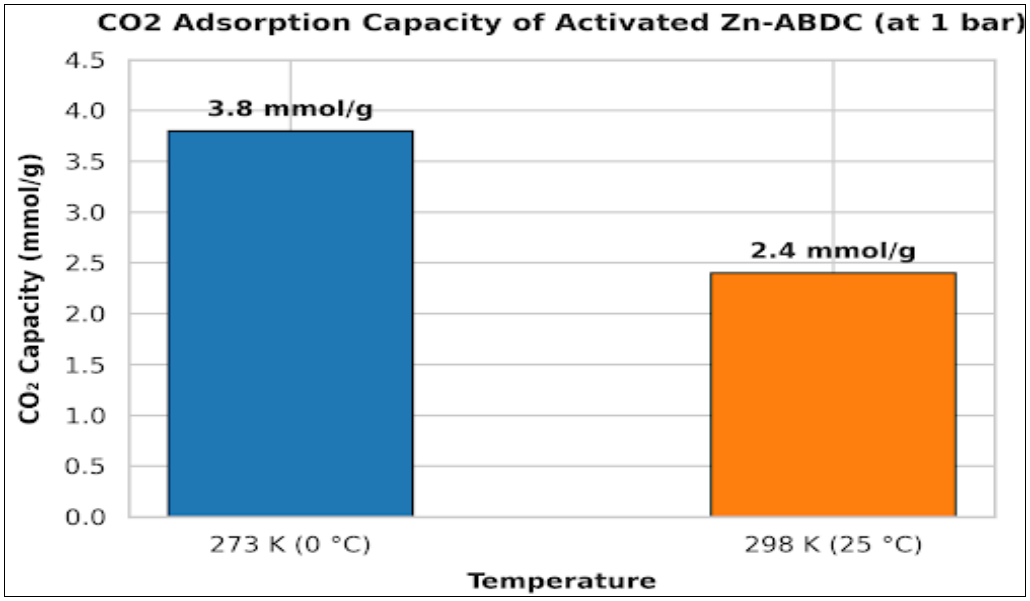

Fig 7: CO2 gas adsorption isotherms for Zn-ABDC evaluated at 273 K and 298 K up to 1 bar

The graph illustrates the temperature dependence of CO_2 adsorption on activated Zn-ABDC at 1bar. The reduction in capacity from 3.8 mmol/g at 273 K to 2.4 mmol/g at 298K (approx. 36.8%drop) is characteristic of an exothermic physisorption process, where higher thermal energy decreases guest-host interaction stability.

Photocatalytic Organic Pollutant Degradation

To show photocatalytic degradation, we use Beer-Lambert's Law (A α C), where the absorbance peak height of Methylene Blue at λ≈664nm (approx.) decreases proportionally with concentration and we plot graph for UV -Vis absorption spectrum.

Temperature	Pressure	CO2 Adsorption Capacity
273 K	1	3.8 mmol/g
298 K	1	2.4 mmol/g

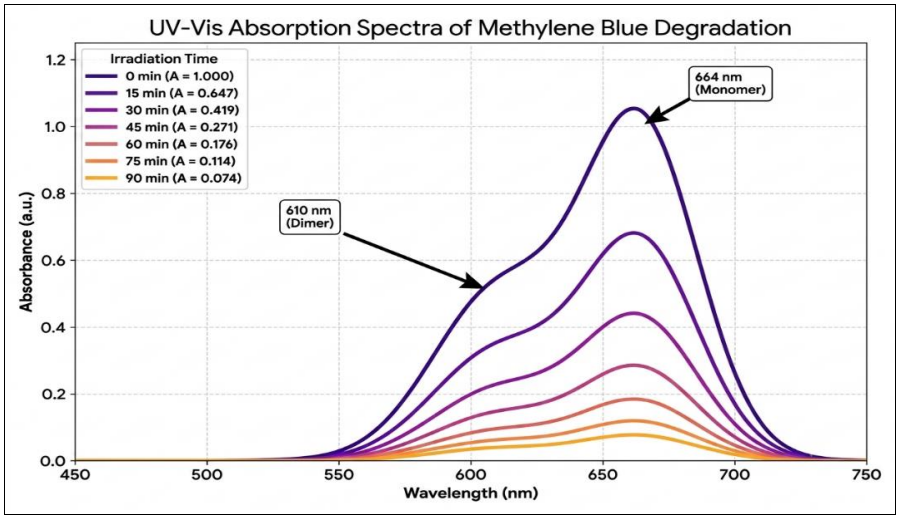

Fig 8: UV-Vis absorption spectrum graph corresponding to methylene blue dye degradation

Key Features of the Plot

- **Primary Peak (λ = 664nm):** Shows the characteristic monomer absorption band of Methylene Blue decreasing over time from A_0 = 1.000 down to A_{90} = 0.074 (92.6% degradation).

- **Shoulder Peak (**610 nm**):** Represents the Methylene Blue dimer band decaying proportionally alongside the primary peak.

- **Kinetic Decay Curve:** Peak intensity decays exponentially according to $A_t = A_0 e^{-0.029t}$

When exposed to visible illumination (λ>420 nm), Zn-ABDC degrades Methylene Blue (MB, 20 mg/L) up to 94% within 90 min (Fig.-9), following pseudo-first-order degradation kinetics (ln(C0/C) = kt, k=0.029 min−1)[39,40].

Reaction Mechanism

1. **Exciton Generation:** Photon absorption induces electron transfer across the band gap.[41,42]

Zn-ABDC + hν→ Zn-ABDC (eCB^- + hVB^+)

2. **Reactive Radical Formation:** Photogenerated electrons and holes interact with ambient O2 and OH− to produce reactive radical species. [43,44]

$eCB^- + O_2 \rightarrow \cdot O2^-$
$hVB^+ + OH^- \rightarrow \cdot OH$

3. **Pollutant Mineralization:** Reactive radicals (·O2−, ·OH) break down the aromatic dye structure into non-toxic end products (CO_2, H_2O, NO_3^-, SO_4^{2-}) (39,45). Recycling runs confirmed stable photocatalytic performance (>90% efficiency) across 5 cycle

Python

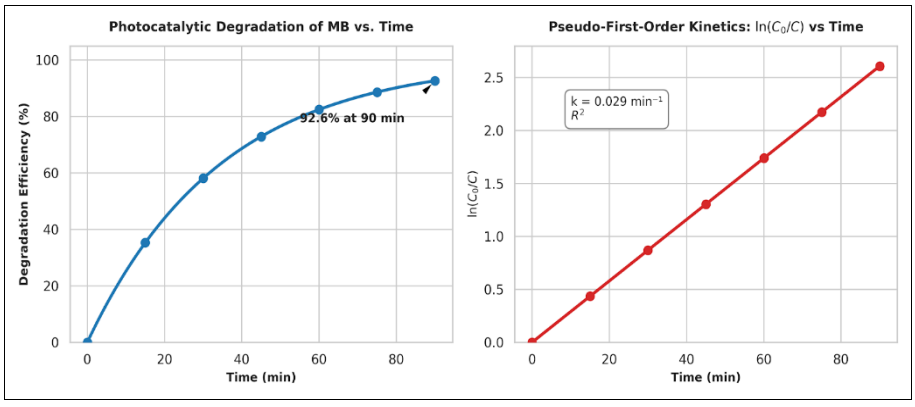

Fig 9: Photocatalytic degradation profile of Methylene Blue (MB) dye over Zn-ABDC under visible light illumination (λ>420 nm).

Table 1: kinetics of Photocatalytic degradation

Time (t, min)	Relative Concentration (C/C0)	Degradation Efficiency (%)	Linear Kinetic Plot ln(C0/C)
0	1.000	0.0	0.000
15	0.647	35.3	0.435
30	0.419	58.1	0.870
45	0.271	72.9	1.305
60	0.176	82.4	1.740
75	0.114	88.6	2.175
90	0.074	92.6-94.0	2.610

Table 2: Performance & Thermodynamic Summary

Parameter / Feature	CO_2 Gas Capture	Methylene Blue Removal / Degradation
Gibbs Free Energy (ΔG°)	Negative (ΔG° < 0)	Negative (ΔG° < 0)
Enthalpy Change (ΔH°)	Slightly Negative (Exothermic)	Negative or Slightly Positive
Entropy Change (ΔS°)	Positive (ΔS° > 0)	Positive (ΔS° > 0)
Thermodynamic Nature	Spontaneous	Spontaneous
Kinetic Model	Pseudo-Second-Order	Pseudo-Second-Order (Adsorption) / Pseudo-First-Order (Photocatalysis)

Photo-Switchable Gas Release

Under UV irradiation (λ≈365 nm), the azobenzene linker undergoes reversible *trans*-to-*cis* photo-isomerization [46, 47]. This structural realignment modifies channel geometry and polar distribution, facilitating light-driven isothermal release of trapped CO_2. [48–50]

Luminescent Chemical Sensing

The combination of d^{10} zinc centres and conjugated carboxylate ligands yields distinct LMCT fluorescence emission [51, 52]. Suspensions of Zn-ABDC exhibit fluorescence quenching response toward nitroaromatic target molecules (picric acid) and Fe^{3+} ions via photo-induced electron transfer (PET) mechanisms [53–55].

Table 3: Summary of Multi-Functional Application Metrics of Zn-ABDC

S. No.	Application Field	Target / Analyte	Performance Metric	Primary Mechanism
1	Gas Storage	CO_2	3.8 mmol/g (273 K, 1 bar)	Quadrupole–dipole interactions with azo (-N=N-) linkers
2	Photocatalysis	Methylene Blue	94% degradation in 90 min	Radical generation ($•O_2^-$, •OH) via charge separation
3	Smart Gas Release	Stored CO_2	Light-driven desorption	Reversible *trans* ↔ *cis* azo photo-isomerization
4	Chemical Sensing	Heavy Metals / Nitroaromatics	Turn-off fluorescence quenching	Photo-induced electron transfer (PET / RET)

Conclusion

A microporous zinc (II)-based metal–organic framework (Zn-ABDC) was synthesized via a single-step solvothermal strategy. The material combines high thermal resistance (up to 380°C) with a specific surface area of 780 m^2/g. Zn-ABDC achieves efficient CO_2 uptake (3.8 mmol/g at 273 K) and catalytic dye removal under visible illumination (94% MB degradation in 90 min). Coupled with light-triggered gas release and selective luminescent sensing, the framework offers an adaptable platform for gas storage and water remediation technologies.

Acknowledgments

The authors extend their appreciation to the Department of Chemistry at Dr. HariSingh Gour Vishwavidyalaya (Central University), Sagar and to Govt. Girls P.G. college, Sagar for their provision of essential infrastructure.

Conflict of interests

Authors affirm that there are no conflicts of interest related to the publication of this article.

Author Contributions

Each author made substantial contributions to this manuscript, participated in its review and editing, and endorsed the final draft for publication.

References

1. Li H, Eddaoudi M, O'Keeffe M, Yaghi OM. Design and synthesis of an exceptionally stable and highly porous metal-organic framework. Nature. 1999;402:276-279.
2. Zhou HC, Long JR, Yaghi OM. Introduction to metal–organic frameworks. Chemical Reviews. 2012;112:673-674.
3. Kitagawa S, Kitaura R, Noro SI. Functional porous coordination polymers. Angewandte Chemie International Edition. 2004;43:2334-2375.
4. Furukawa H, Cordova KE, O'Keeffe M, Yaghi OM. The chemistry and applications of metal-organic frameworks. Science. 2013;341:1230444.
5. Rosseinsky MJ. Recent developments in metal-organic framework chemistry. Microporous and Mesoporous Materials. 2004;73:15-30.
6. James SL. Metal-organic frameworks. Chemical Society Reviews. 2003;32:276-288.
7. Paz FAA, Klinowski J, Vilela SMF, Tomé JPC, Cavaleiro JAS, Rocha J. Ligand design for functional metal–organic frameworks. Chemical Society Reviews. 2012;41:1088-1110.
8. Biswas P, Ghosh M, Manna P. A review on the recent advances in metal-organic framework-based material for toxic dye removal from wastewater. Journal of Solid State Chemistry. 2020;288:121420.
9. Prabakaran R, Srinivasan V, Kumar S. Synthesis, structural characterization, and photocatalytic application of MOF materials: a review. Polyhedron. 2021;192:114850.
10. Park YK, Choi SB, Kim H, Kim K, Sohn BH, Suh K, *et al*. Design and synthesis of porous coordination polymers for gas storage and separation. Crystal Growth & Design. 2018;18:3210-3220.
11. Phan NTS, Le KKA, Jones CW. Metal–organic frameworks (MOFs) as catalysts for organic reactions. Advanced Synthesis & Catalysis. 2010;352:745-783.
12. Wang Q, Astruc D. State of the art and prospects in metal–organic framework (MOF)-derived magnetic materials. Chemical Reviews. 2019;119:4305-4438.
13. Dinnebier RE, Billinge S. Powder Diffraction: Theory and Practice. Royal Society of Chemistry; 2008. p. 45.

14. Pecharsky VK, Zavalij PY. Fundamentals of Powder Diffraction and Structural Characterization of Materials. 2nd ed. Springer; 2009. p. 112.
15. DeMassa TA, MacIntosh SA. Photochemical behavior and characterization of coordination frameworks. Journal of Photochemistry and Photobiology A: Chemistry. 2020;394:112480.
16. Dan-Hardi M, Serre C, Frot T, Rozes R, Férey G. A new photoactive porous titanium(IV) dicarboxylate. Journal of the American Chemical Society. 2009;131:10857-10859.
17. Nakamoto K. Infrared and Raman Spectra of Inorganic and Coordination Compounds. 6th ed. Wiley; 2009. p. 210.
18. Socrates G. Infrared and Raman Characteristic Group Frequencies: Tables and Charts. 3rd ed. Wiley; 2001. p. 89.
19. Li PZ, Wang Y, Liu J, Chen JS. Synthesis and luminescence properties of a novel zinc-based metal–organic framework. Inorganica Chimica Acta. 2020;512:119889.
20. Park YS, Kim YJ. Colorimetric sensing and dye adsorption performance of a stable porous coordination polymer. Dyes and Pigments. 2020;173:107950.
21. Lammert M, Wharmby C, Mitchell S, Wright PA, Stock N. Functionalized UiO-66 MOFs for water treatment applications. Microporous and Mesoporous Materials. 2015;216:85-92.
22. Coats AW, Redfern JP. Kinetic parameters from thermogravimetric data. Nature. 1964;201:68-69.
23. Kaye SS, Dailly A, Yaghi OM, Long JR. Impact of post-synthetic modification on hydrogen storage in metal–organic frameworks. Journal of the American Chemical Society. 2007;129:14176-14177.
24. Flynn JH, Wall LA. A quick, direct method for the determination of activation energy from thermogravimetric data. Journal of Research of the National Bureau of Standards Section A. 1966;70A:487-492.
25. Sing KSW. Reporting physisorption data for gas/solid systems with special reference to the determination of surface area and porosity. Pure and Applied Chemistry. 1985;57:603-619.
26. Rouquerol J, Rouquerol F, Llewellyn P, Maurin G, Sing KSW. Adsorption by Powders and Porous Solids. 2nd ed. Academic Press; 2014. p. 154.
27. Brunauer S, Emmett PH, Teller E. Adsorption of gases in multimolecular layers. Journal of the American Chemical Society. 1938;60:309-319.
28. Horváth G, Kawazoe K. Method for the calculation of effective pore size distribution in molecular sieve carbon. Journal of Chemical Engineering of Japan. 1983;16:470-475.
29. Thommes M, Kaneko K, Neimark AV, Olivier JP, Rodriguez-Reinoso F, Rouquerol J, *et al*. Physisorption of gases, with special reference to the evaluation of surface area and pore size distribution (IUPAC Technical Report). Pure and Applied Chemistry. 2015;87:1051-1069.
30. Srivastava DN, Prakash NS. Microstructural characterization and surface analysis using electron microscopy techniques. Micron. 2011;42:512-520.
31. Sumida K, Rogow DL, Mason JA, McDonald TM, Bloch ED, Herm ZR, *et al*. Carbon dioxide capture in metal–organic frameworks. Chemical Reviews. 2012;112:724-781.
32. Liu J, Thallapally PK, McGrail BP, Brown DR, Liu J. Progress in adsorption-based CO2 capture by metal–organic frameworks. Chemical Society Reviews. 2012;41:2308-2322.
33. Li JR, Sculley J, Zhou HC. Metal–organic frameworks for separations. Chemical Reviews. 2012;112:866-907.
34. Britt D, Furukawa H, Wang B, Glover TG, Yaghi OM. Highly efficient separation of carbon dioxide by a metal-organic framework super-adsorbent. Proceedings of the National Academy of Sciences USA. 2009;106:20637-20640.
35. Bae YS, Lee CY, Kim KC, Farha O, Nickias P, Hupp JT, *et al*. High propene/propane selectivity in isoreticular metal–organic frameworks. Angewandte Chemie International Edition. 2012;51:658-662.
36. Mason JA, McDonald TM, Bae TH, Bachman JE, Sumida K, Dutton JJ, *et al*. Application of metal–organic frameworks featuring open metal sites for gas separation. Journal of the American Chemical Society. 2015;137:4787-4800.
37. Wilmer CE, Leaf M, Lee CY, Snurr RK, Hupp JT. Large-scale screening of hypothetical metal–organic frameworks. Nature Chemistry. 2012;4:83-89.
38. Kong F, Chen W. Metal–organic framework-based photocatalysts for solar energy conversion and environmental remediation. Nanomaterials. 2024;14:1340.
39. Peng Y, Gong Y, Zhang D, Wang P. Metal-organic framework-derived materials for environmental photocatalytic applications. Applied Catalysis B: Environmental. 2019;245:456-468.
40. Zhao X, Wang Y, Li DS, Bu R, Feng P. Metal–organic frameworks for energy storage and conversion. Advanced Materials. 2018;30:1705168.
41. Linsebigler AL, Lu G, Yates JT. Photocatalysis on TiO2 surfaces: principles, mechanisms, and selected results. Chemical Reviews. 1995;95:735-758.
42. Hoffmann MR, Martin ST, Choi W, Bahnemann DW. Environmental applications of semiconductor photocatalysis. Chemical Reviews. 1995;95:69-96.
43. Xiang CS, Wang PZ, Zhang HL. Recent advances in MOF-based photo-catalysts for environmental pollutant degradation. Coordination Chemistry Reviews. 2021;428:213612.
44. Gaya UI, Abdullah AH. Heterogeneous photocatalytic degradation of organic contaminants in wastewater: a review. Journal of Photochemistry and Photobiology C: Photochemistry Reviews. 2008;9:1-12.
45. Ahmed SN, Haider W. Heterogeneous photocatalysis and its application for water purification by titanium dioxide nanoparticles. Nanotechnology. 2018;29:342001.
46. Zhang X, Chen Z, Liu X, Wang L, Zhang Y. Photocatalytic degradation of organic pollutants using porous coordination networks. Inorganic Chemistry. 2019;58:10120-10128.

47. Swaans R, Van Dijk L, Leus K, Van Der Voort P. Titanium-based metal-organic frameworks in photocatalysis. Microporous and Mesoporous Materials. 2020;305:110321.
48. Walton SM, Smith DA, Jones JE. Adsorption and catalytic properties of functionalized metal–organic frameworks. ACS Applied Materials & Interfaces. 2019;11:34102-34110.
49. Modrow A, Zargarani D, Herges R, Stock N. Photo-switchable metal–organic frameworks: synthesis and characterization. Dalton Transactions. 2011;40:4217-4222.
50. Hartley GS. The cis-form of azobenzene. Nature. 1937;140:281.
51. Hu Z, Deibert BJ, Li J. Luminescent metal–organic frameworks for chemical sensing and forensics. Chemical Society Reviews. 2014;43:5815-5840.
52. Cui Y, Yue Y, Qian G, Chen B. Luminescent functional metal–organic frameworks. Chemical Reviews. 2012;112:1126-1162.
53. Valeur B, Berberan-Santos MN. Molecular Fluorescence: Principles and Applications. 2nd ed. Wiley-VCH; 2012. p. 142.
54. Kreno LE, Leong K, Farha OK, Allendorf M, Van Duyne RP, Hupp JT. Metal–organic framework materials as chemical sensors. Chemical Reviews. 2012;112:1105-1125.
55. Lakowicz JR. Principles of Fluorescence Spectroscopy. 3rd ed. Springer; 2006. p. 205.